Chapter 5

Effect of Doping and Codoping on Microstructure and Physical Property of ZnO

CHAPTER-5
Effect of Doping and Codoping on Microstructure and Physical Property of ZnO

In this chapter, we have probed the effect of doping and/or codoping on microstructure and physical properties like optical as well as magnetic. The microstructure and magnetic properties of Co doped ZnO have been studied by our group earlier [Rath *et al*. (2009)]; here we have studied the doping of Mg and codoping with Mg and Co. We have synthesised $Zn_{1-x}Mg_xO$ nanoparticles with varying x = 0, 0.04, 0.08, 0.12, 0.10 and 0.15 and explained the microstructural changes with respect to Mg concentration. The results are discussed in Section 5.1. Microstructure dependent optical and magnetic properties of Mg and/or Co doped/codoped ZnO samples with varying Mg and Co concentration are discussed in Section 5.2. Finally the conclusions are given in Section 5.3.

5.1 Mg Doped ZnO

5.1.1 Microstructure

X-ray diffraction pattern of pure and $Zn_{1-x}Mg_xO$ ($0.04 \leq x \leq 0.20$) are depicted in Fig. 5.1. Upto x=0.15 of Mg doping, all observed peaks are indexed with the wurtzite phase (JCPDS 89-1397) of ZnO. No additional peaks within the detection limit of XRD is observed indicating neither any structural changes nor formation of additional phases in ZnO upto x=0.15. $Mg(OH)_2$ (JCPDS 07-0239) as an impurity phase is observed at x=0.20. The solubility limit of Mg in ZnO is ≤ 0.20, which is higher than the reported value [Kumar *et al*. (2012); Ohtomo *et al*. (1999)]. XRD peak corresponding to (101) plane with increasing Mg concentration shifts towards higher 2θ value indicating the decrease in lattice parameter, shown in Fig. 5.1 (right side). We have analysed the lattice parameters and found a decrease in c/a ratio with increase in 'x' ($0 \leq x \leq 0.20$) by using Fullprof software for Le-Bail refinement at constant scale factor, shown in Fig. 5.2 and the results are compiled in Table. 5.1. Further, the strain

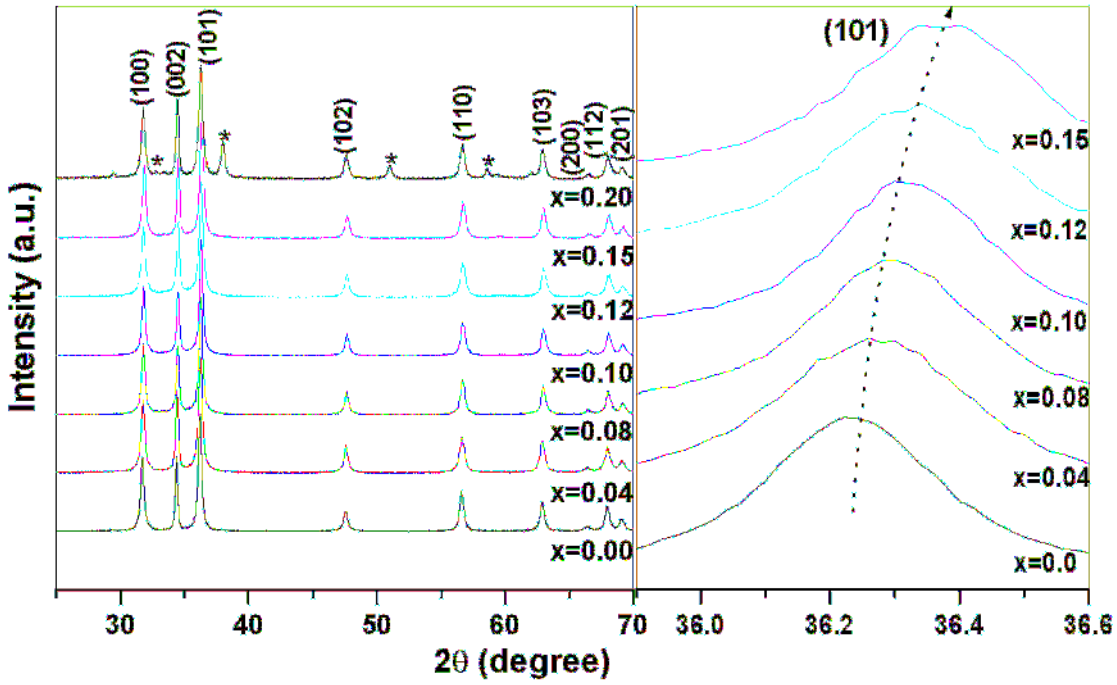

Figure 5.1: X-ray diffraction pattern of $Zn_{1-x}Mg_xO$ (x = 0, 0.04, 0.08, 0.10, 0.12, 0.15 and 0.20) nanoparticles.

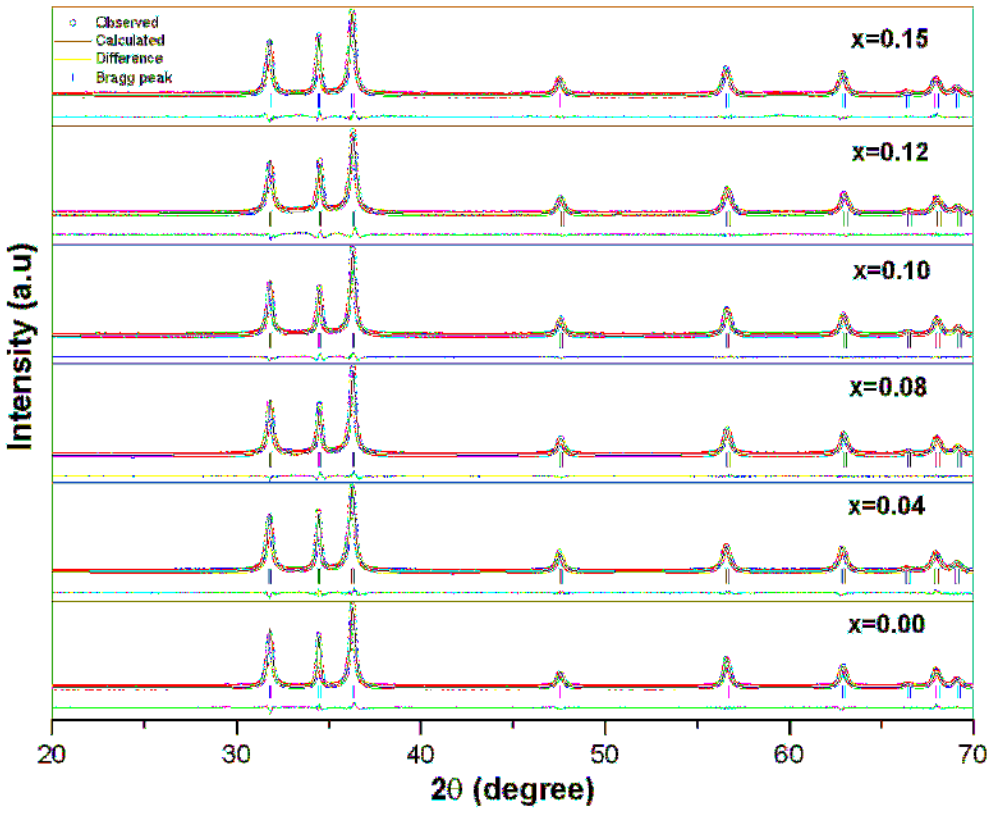

Figure 5.2: Le-Bail refinements of X-ray diffraction pattern for $Zn_{1-x}Mg_xO$ (x = 0, 0.04, 0.08, 0.12, 0.10 and 0.15) nanoparticles.

and particle size are calculated from the W–H plot as shown in Fig. 5.3. Strain and particle size with varying the x ($0 \leq x \leq 0.20$) are tabulated in Table 5.1. With increase in x ($0 \leq x \leq 0.20$), strain from W-H plot as well as c/a ratio obtained from Le Bail profile fitting confirm the reduction of defects in the lattice. The particle size of ZnO is reduced from 11 nm to 7 nm upon Mg doping irrespective of dopant concentration.

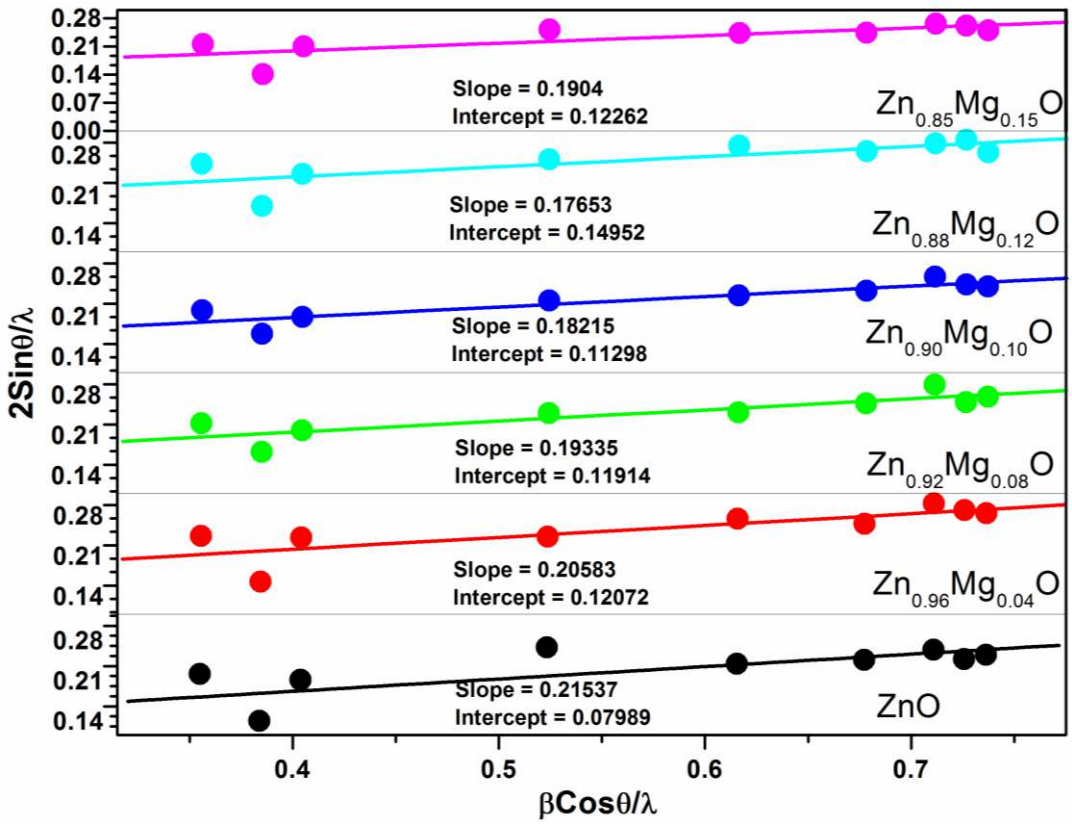

Figure 5.3: W-H plot for $Zn_{1-x}Mg_xO$ (x = 0, 0.04, 0.08, 0.10, 0.12 and 0.15) nanoparticles.

Fig. 5.4(a-b) depicts typical TEM micrograph with EDS pattern of ZnO and $Zn_{0.96}Mg_{0.04}O$ samples. The corresponding EDS spectra confirm the presence of Mg in $Zn_{0.96}Mg_{0.04}O$. Selected area electron diffraction (SAED) pattern of both the samples reveal self-organisation of nanoparticles and their single crystalline nature. While the homogeneous particle size distribution with size about 18 nm in ZnO is observed, in $Zn_{0.96}Mg_{0.04}O$ sample, a broad size distribution of nanorods having aspect ratio 1:4 are detected.

Table 5.1. The c/a ratio and lattice volume detection from Le-Bail refinement, Particle size and strain calculation from the W-H plot.

Sample name (P 63 m c)	c/a	Volume	Strain	Particle Size (D)
089-1397	1.6025	47.77	---------	------
ZnO	1.6022	47.5908	0.21537	11.27
$Zn_{0.96}Mg_{0.04}O$	1.6017	47.6761	0.20583	7.46
$Zn_{0.92}Mg_{0.08}O$	1.6010	47.5236	0.19335	7.55
$Zn_{0.90}Mg_{0.10}O$	1.6009	47.5382	0.18215	7.97
$Zn_{0.88}Mg_{0.12}O$	1.6005	47.4839	0.17653	6.02
$Zn_{0.85}Mg_{0.15}O$	1.6018	47.6685	0.1904	7.34

a, b, and c are in A^o, (D is in nm)

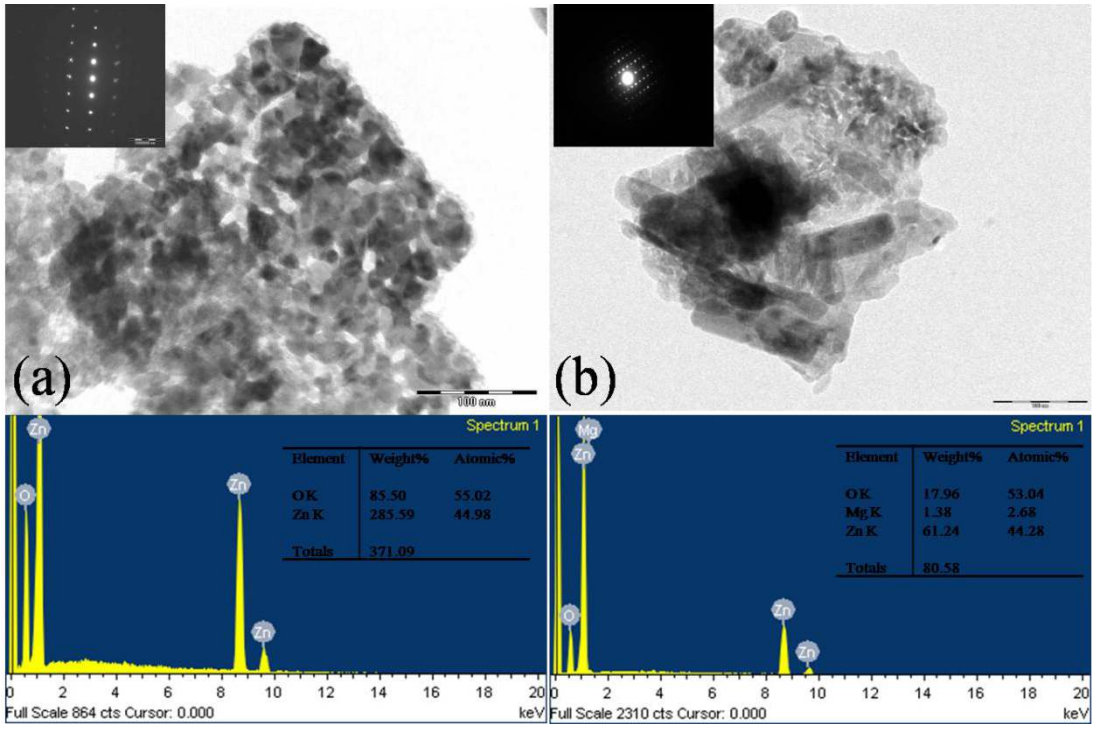

Figure 5.4: Transmission Electron Micrograph of **(a)** ZnO and **(b)** $Zn_{0.96}Mg_{0.04}O$ nanoparticles with corresponding EDS spectra. Inset shows the SAED pattern of respective samples.

5.1.2 Optical Properties

Typical photoluminescence spectra of ZnO and $Zn_{0.96}Mg_{0.04}O$ are shown in Fig. 5.5. One intense emission peak at about 3.2 eV and a broad hump in the range of 2.4 to 1.8 eV for an excitation wave length 266 nm have been seen. UV emission at 3.2 eV is due to the recombination of free excitons and is known as near band edge (NBE) emission. It has been reported by Ke *et al.* (2010) that optical transition occurs in green (2.32 eV), green-yellow (2.21 eV) and yellow-orange (2.07 eV) zones for ZnO. While green emission is ascribed to Zn vacancies, green-yellow emission is likely due to O vacancies and yellow-orange emission may be caused by O interstitials [Ke et al. (2010)]. Therefore, the latter broad emission could be mediated by some deep level defects or vacancies due to impurities in the present case. However, Mg inclusion suppresses the broad emission. Improvement in UV emission

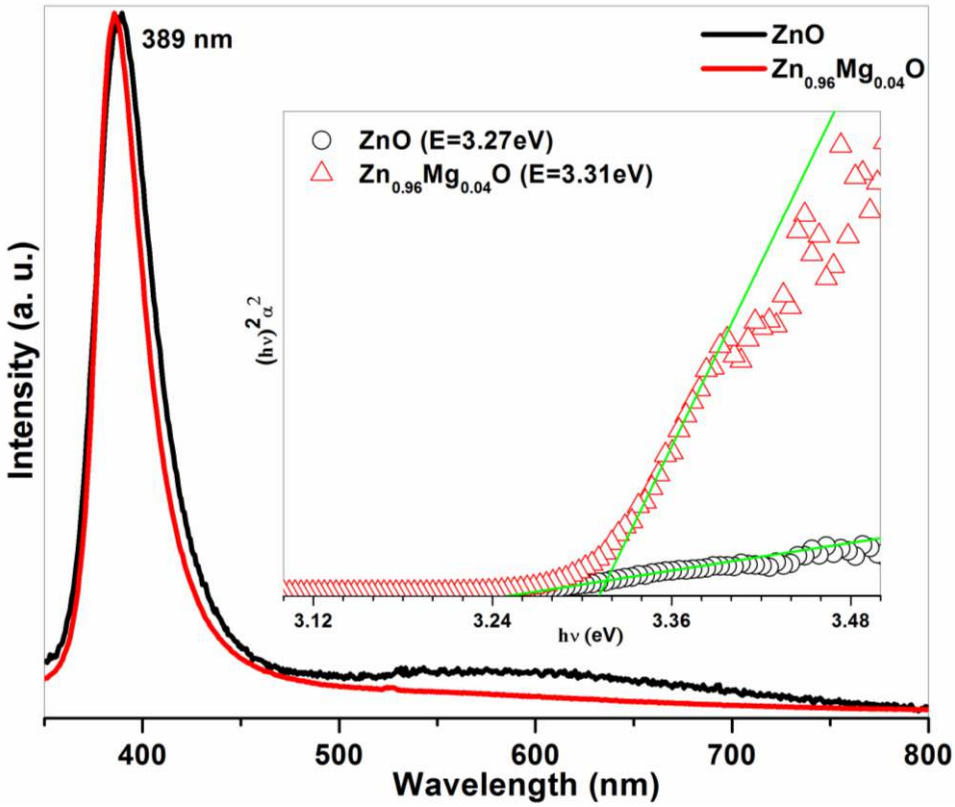

Figure 5.5: Photo luminescence spectrum of ZnO and $Zn_{0.96}Mg_{0.04}O$ nanoparticles. Inset shows the plot of $(\alpha hv)^2$ vs. hv of both samples obtained from UV-visible spectrum.

(3.2 eV) efficiency of Mg doped ZnO is ascribed to the diminution of active centres, which are responsible for the origin of visible emission [Ohashi *et al.* (2003)]. Near band edge emission is well matched with the optical band gap obtained from UV-visible spectroscopy. A clear shift in absorption onset towards blue is observed in Mg doped ZnO (inset of Fig. 5.5), indicating an increase in band gap. Thus PL studies clearly show the reduction or passivation of native defects in $Zn_{0.96}Mg_{0.04}O$ nanoparticles compared to ZnO.

5.1.3 Detection of Vibrational Modes

Fig. 5.6 shows the Raman spectra of ZnO and $Zn_{0.96}Mg_{0.04}O$ nanoparticles ranging from 300 to 1400 cm^{-1} measured at room temperature. Due to overlapped modes, we could not distinguish the individual peaks. The whole spectra are thus deconvoluted into separate peaks by Lorentzian curve fitting shown as insets of Fig. 5.6. It is clearly seen that reported values of first order Raman modes such as $A_1(TO)$, $E_1(TO)$, $E_2(high)$, $A_1(LO)$, $E_1(LO)$ and second order mode such as $2E_2$ are matched well with the experimentally observed Raman modes [Manjón *et al*. (2005); Decremps *et al*. (2002); Cuscó *et al*. (2007)]. Besides the first order and second order phonon modes, a few additional modes at about 517, 536, and 649 cm^{-1} are also observed [Manjón *et a*l. (2005); Decremps *et al*. (2002); Cuscó *et al*. (2007)]. Additional modes in both pure and doped ZnO in our case are matched with the silent modes of ZnO [Wang *et al*. (2007); Bundesmann *et al*. (2003)]. However, the intensity of these modes decreases in $Zn_{0.96}Mg_{0.04}O$. After deconvolution, the broad band in the range 900 to 1250 cm^{-1}, is fitted with four peaks in ZnO at positions 982, 1050, 1096 and 1148 cm^{-1} as well as in $Zn_{0.96}Mg_{0.04}O$ centred at 974, 1053, 1099 and 1148 cm^{-1} represent the multiphonon modes and are matched well with reported values [Manjón *et al*. (2005)]. The peaks at 583 and 1148 cm^{-1} are assigned as first order and second order of $E_1(LO)$ mode respectively as a consequence of defects such as O-vacancies, Zn interstitials, or these complexes [Pradhan *et al.* (2004)]. The ratio of $E_1(LO)$ and $E_{2,High}$ (characteristic of wurtzite structure); which tells quantitatively about the

presence of defects are found to be higher in ZnO than in $Zn_{0.96}Mg_{0.04}O$, well corroborates with the PL results.

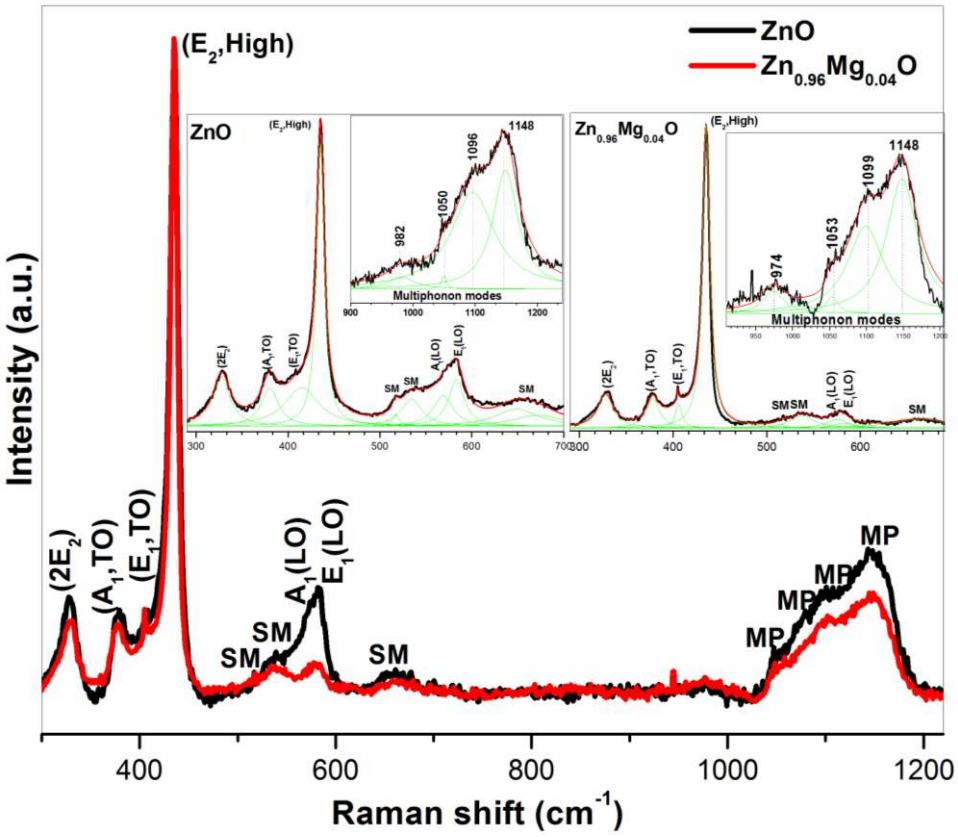

Figure 5.6: Raman spectrum of ZnO and $Zn_{0.96}Mg_{0.04}O$ nanoparticles in the range of 300 to 1400 cm^{-1}. Inset shows the Lorentzian fitting of 270-760 cm^{-1} and 900-1240 cm^{-1} for respective samples.

Atomic vibrational modes of pure and Mg doped ZnO are examined by FTIR as shown in Fig. 5.7. Peak at around 2363 cm^{-1} is caused by a small amount of residual CO_2. Two peaks observed at 1261 and 1385 cm^{-1} correspond to residual NO_3^- ion which could not be removed completely after washing. A broad band between 400 and 650 cm^{-1} represents the stretching mode of Zn-O [Gayen *et al*. (2008); Noei *et al*. (2008)]. The band centred at 1620 cm^{-1} is the bending vibrational mode of hydroxyl group of the chemisorbed and/or physiosorbed water molecules [Noei *et al*. (2008)]. A broad band around 3000-3700 cm^{-1} corresponds to the O-H bond stretching local vibrational modes (LVM). After deconvolution of broad band, peaks at

3251, 3384, 3452, 3492, 3532 and 3575 cm^{-1} have been obtained in ZnO and Mg doped ZnO (Fig. 5.7 (right)). The peaks are assigned to interstitial hydrogen bonded with oxygen in bond-center and anti-bonding position as well as with vacant zinc site (V_{Zn}) in parallel and perpendicular alignment to the c-axis. The observed modes are compared with both theoretically and experimentally reported values and are found to lie in between both these limits [Wardle *et al*. (2005); Park *et al*. (2008)]. A prominent band at 908cm^{-1} observed in ZnO corresponds to the bending vibration of V_{Zn}-$H_{ABO\parallel}$ [Wardle *et al*. (2005)]. Besides the above common modes, a few additional modes are also observed at 856, 1512 and 3690 cm^{-1} in Mg doped ZnO. These bands become more pronounced with higher concentration of Mg. All three modes scale in intensity with Mg content which further indicates that the above modes are due to vibrations of different Mg–H complexes. Local vibrational modes of the Mg_{Ga}-H complexes have also been identified through infrared absorption

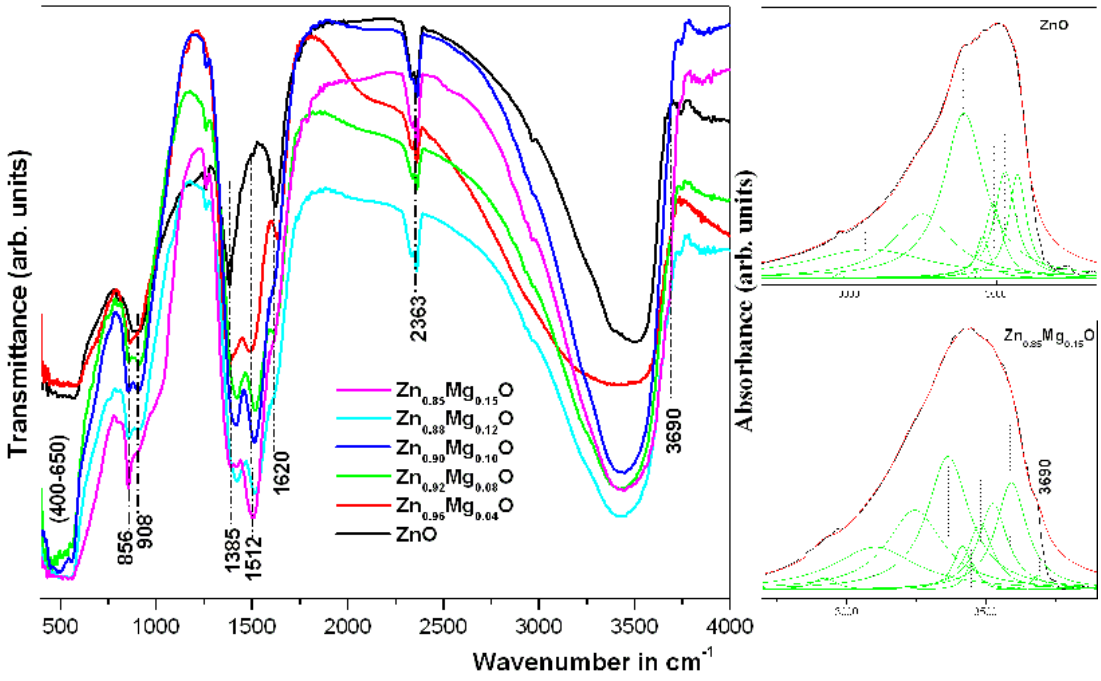

Figure 5.7: FT-IR transmittance spectram of $Zn_{1-x}Mg_xO$ (x = 0, 0.04, 0.08, 0.10, 0.12 and 0.15) nanoparticles (left side). The absorbance plot for the ZnO and $Zn_{0.85}Mg_{0.15}O$ nanoparticles in range of 2500-3900 cm^{-1}, with Lorentzian fitting, is shown in right side.

measurements in Mg doped GaN at 3125 cm^{-1} [Cusco *et al*. (2004)]. Gonzalez *et al*. (1981) have reported Mg-H band at 1000cm^{-1} and a band at 3700 cm^{-1} for $Mg(OH)_2$ precipitates in MgO. One may clearly see in our case that the peaks at 908 cm^{-1} and 1512 cm^{-1} in ZnO are splitted into two peaks after Mg doping. Therefore, the additional mode at 856 cm^{-1} could be attributed to Mg-H and modes at 1512 and 3690 cm^{-1} to Mg-OH band. The amount of hydrogen impurity is thus found to be higher in Mg doped ZnO. This is possible due to high hydrogen storage capacity of Mg [Yu *et al*. (1988)]. Similar occurrence of higher hydrogen content in $Zn_{0.96}Mg_{0.04}O$ nanowire than that of ZnO nanowire have been found by Pan *et al.* (2006) through hydrogen absorption measurements. Gonzalez *et al.* (1981) have reported that if hydrogen impurities are present in the crystal, it is expected that they can be trapped at oxygen-vacancy sites and form H^- ions. Gotz *et al.* (1996) have also established in Mg doped GaN that Mg acceptors are passivated by hydrogen. Thus, one expects the excess hydrogen in Mg doped ZnO may passivate more vacancies compared to pure ZnO and results in less native defects contributing to defect emission in PL spectrum as observed in our case.

5.1.4 Detection of Cationic Defects

Positron annihilation measurement is further used as a complementary technique to further probe the defects, shown in Fig. 5.8. The positron annihilation life time τ_1 is 150 ps for $Zn_{0.96}Mg_{0.04}O$ which is lower than that of τ_1 (186ps) of ZnO nanoparticles and is comparable to that of bulk ZnO (158 ps). It has been calculated theoretically that if hydrogen is attached to V_{Zn}, the positron life time decreases successively [Brauer *et al.* (2009); Anwand *et al.* (2010)]. For example, while a hydrogen attached to V_{Zn} yields a positron life time of ~200 ps while four hydrogens attached to zinc vacancy reduces the life time to 158-162 ps [Brauer *et al*. (2009); Anwand *et al*. (2010)]. Therefore, τ_1 in ZnO and $Zn_{0.96}Mg_{0.04}O$ matches well with the life time of V_{Zn} attached to one and four hydrogens respectively which further support the FTIR results. Depending upon the size, vacancies could be a cluster of 2 to 6 di-vacancies

(V_{Zn+O}) and subsequently the life time of positron annihilation increases from 265 ps to 375 ps [Chen *et al.* (2004)]. The life time 368 ps obtained for τ_2 in ZnO is in between the life time of positron annihilation corresponding to cluster of 5 and 6 (Zn+O) di-vacancies. However, in $Zn_{0.96}Mg_{0.04}O$, the decrease in τ_2 (306 ps) value further indicates the passivation of divacancies by hydrogen or the reduction in the size of Zn+O divacancies. From this study, we conclude that the native defects in ZnO are significantly reduced or passivated by Mg doping [Brauer *et al.* (2009)]. Hydrogen is responsible for the passivation of such defects and the formation of V_{Zn}-H and Mg-H type of defect complexes.

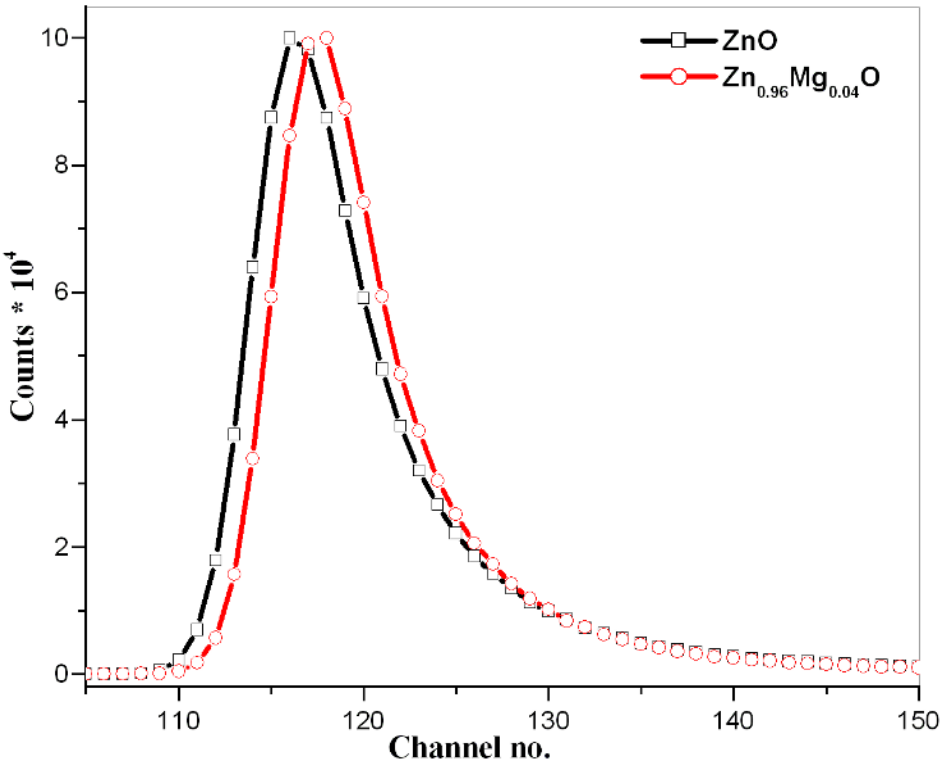

Figure 5.8: Positron lifetime spectrum of ZnO and $Zn_{0.96}Mg_{0.04}O$ nanoparticles.

5.1.5 Chemical Bonding

To understand the chemical bonding in ZnO and $Zn_{1-x}Mg_xO$ nanopowders, the core levels of Zn 2p, Mg 1s and O 1s states are examined using XPS techniques as shown in Fig. 5.9(a-c), respectively. In ZnO sample,

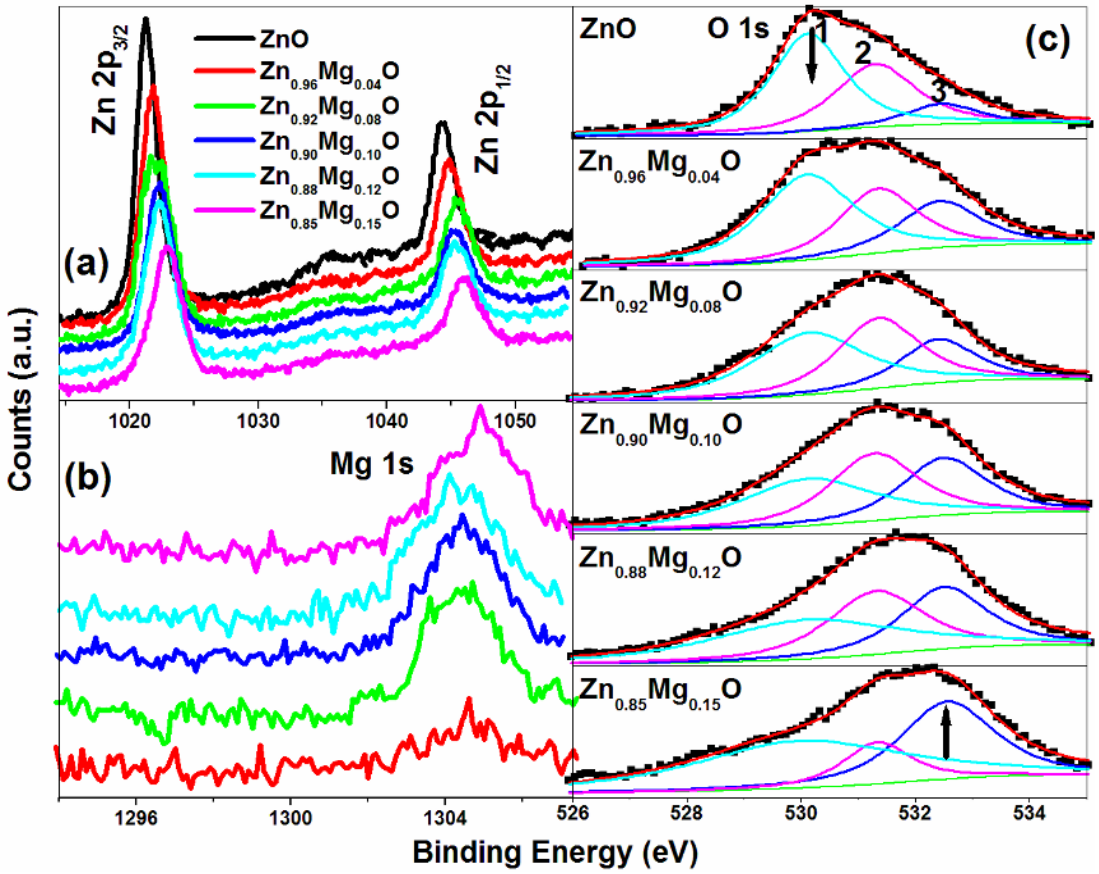

Figure 5.9: XPS spectrum of $Zn_{1-x}Mg_xO$ (x = 0, 0.04, 0.08, 0.10, 0.12 and 0.15) nanoparticles **(a)** For Zn $2p_{3/2}$ and $2p_{1/2}$, **(b)** For Mg 1s and **(c)** For O 1s.

the asymmetric O 1s peak is observed with a shoulder towards higher binding energy side. Using the software of XPS Peak Version 4.1, the O 1s peak is deconvoluted into three peaks such as peak 1, 2 and 3 at 530.12, 531.3 and 532.5 eV, respectively. The peak 1 corresponds to the O-Zn bonding, peak 2 is associated with O^{2-} ions in oxygen deficient regions within the matrix of ZnO or the O-H surface adsorbed group on the ZnO surface, whereas the peak 3 is correlated to H/H_2O species [Lu *et al*. (2000); Lin *et al*. (2005); Valtiner *et al*. (2007)]. The deconvolution in other spectra of O 1s peak for $Zn_{1-x}Mg_xO$ ($4 \leq x \leq 0.20$) samples has been done by fixing the peak positions at 530.12, 531.3 and 532.5 eV in order to compare the intensity of individual peak. The asymmetric O 1s peak maxima from lower binding energy side gradually shifts towards the higher binding energy as x increases from 0 to 0.20. The intensity of peak 1 is found to be most intense compared to 2 and 3 peaks in ZnO.

However, with increasing x ($0 \leq x \leq 0.20$), the intensity of peak 3 is gradually increased at the expense of peak 1. The increase in intensity of peak 3 with increasing x, thus confirms the excess H/H_2O species. The binding energies corresponding to 1021.3 eV and 1044.5 eV are attributed to the $2p_{3/2}$ and $2p_{1/2}$ core levels of Zn ions, confirming its divalent nature. With increasing x ($0 \leq x \leq 0.20$), Zn $2p_{3/2}$ and $2p_{1/2}$ peaks shift towards higher binding energy with decrease in relative intensity. The shift indicates the Mg and/or Mg-H incorporation into Zn site [Lin *et al*. (2005); Panigrahy *et al*. (2010)]. The Mg 1s peak centred at 1304.5 eV is ascribed to the presence of Mg^{2+} replacing Zn^{2+}.

ZnO, a well studied n-type semiconductor, shows many vibrational frequencies like H_i at antibonding site (AB_O, $\perp$), H_i at bond centred position ($BC_{\parallel}$), V_{Zn}-H, V_{Zn}-H_2, Zn-H_O and O-H etc whose origins are still puzzling. However, the interaction of ubiquitous impurity like H with ZnO has many important technological implications. For example, H is expected to become an environmentally benign fuel in future and now particles of ZnO can be a potential material for hydrogen sensor. Moreover, ZnO may be considered as a prospective material for hydrogen storage in future. In our present work, we have successively shown that Mg doped ZnO has even more potentiality for storing hydrogen. We have shown clearly the additional vibrational modes at 908 cm^{-1} and 1512 cm^{-1} after Mg doping which is attributed to Mg-H and Mg-OH bond, respectively. The increase in intensity of above bands with increase in Mg concentration further shows the evidence of excess H/H_2O species in XPS spectra. Although the source of hydrogen is due to the adsorption of H_2O on ZnO surface during the synthesis which is dissociated into H^+ and OH^- groups, the above process speeds up with doping Mg in the ZnO lattice. This is because MgO surface is more sensitive for dissociation of H_2O [Langel *et al*. (1995)]. The dissociation of water occurs at the site of the defects rather than physisorption. The defects change the physical and chemical properties and even increase the dissociation energies [Panigrahy *et al.* (2010)]. The defects such as zinc vacancy (V_{Zn}) and cluster of Zn+O di-vacancies (V_{Zn+O}) might be

responsible for dissociation of water in the present case. Therefore, Mg doped ZnO samples synthesized by easy and cost effective conventional coprecipitation technique could be a useful futuristic material for hydrogen storage. In future, we will carry out the hydrogen storage measurement of Mg doped ZnO samples by using a pressure composition isotherm (PCI).

5.2 Co/Mg Doped and Co, Mg Codoped ZnO

5.2.1 Microstructure

The crystal structure and the phase formation of $Zn_{1-x-y}Co_xMg_yO$ (x=0.04,y=0; x=0.04, y=0.05 and x=0, y=0.05) powder samples characterised by XRD reveal a single, polycrystalline, wurtzite structure of ZnO (JCPDS 89-1397). The XRD spectra are shown in Fig. 5.10 with Le-Bail refinement (using Fullprof software suite) at constant scale factor. The observed and calculated data are overlapped and the difference pattern is shown as continuous line below the spectra. No additional peaks are observed indicating that there are no

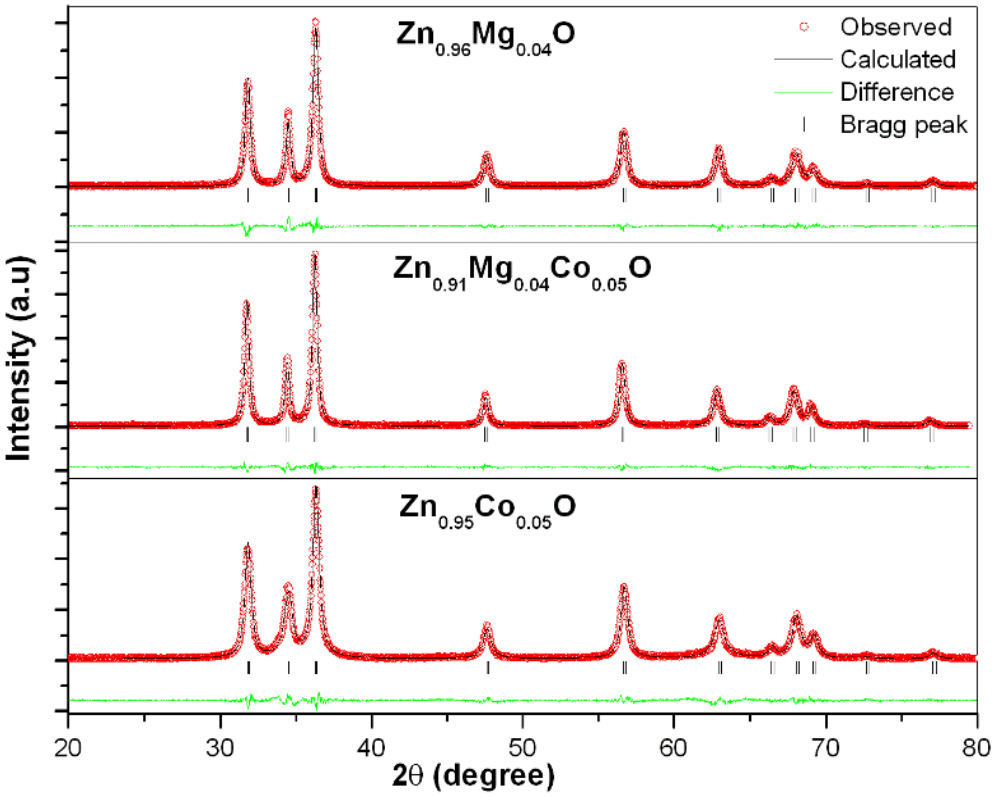

Figure 5.10: Le-Bail refinements of X-ray diffraction pattern for $Zn_{0.95}Co_{0.05}O$, $Zn_{0.96}Mg_{0.04}O$ and $Zn_{0.91}Co_{0.05}Mg_{0.04}O$ nanoparticles.

structural changes and/or formation of additional phases due to the incorporation of Co/Mg or Co and Mg both in ZnO lattice within the detection limit of XRD. Table 5.2 shows the structural parameter, lattice volume and c/a ratio obtained after refinement. It is obvious that one may observe a contraction in lattice parameters after substituting either Mg/Co in place Zn due to their smaller ionic radii. However, when we codoped with Mg and Co, lattice parameters increase and approach the bulk value. The deviation of c/a ratio from the ideal geometry (1.633) indicates the deformed hexagonal lattice under doping. Though, the deformation remains same to that of parent ZnO by doping Co or Mg or Co and Mg both. The crystallite size of doped and co-doped ZnO samples is calculated by using Scherrer formula [Kao *et al*. (2000)] and is depicted in Table 5.2. FE-SEM with corresponding EDS spectra of $Zn_{1-x-y}Co_xMg_yO$ samples are shown in Fig. 5.11(a-c). Incorporation of dopants such as Co, Mg or Co and Mg are shown in the respective EDX spectra but the concentration is found to be less than the exact amount which we have added. Surface morphology is found to be more or less similar in Co and Mg doped sample. Both particles as well as rods are found in the micrographs. Agglomerated particles of size 15-50 nm and nanorods of aspect ratio 1:3 are observed in Mg and Co doped samples. Co and Mg codoped sample clearly shows the presence of nanorods all over the surface with average aspect ratio 1:4.

Table 5.2 Structural parameters of $Zn_{0.95}Co_{0.05}O$, $Zn_{0.96}Mg_{0.04}O$ and $Zn_{0.91}Co_{0.05}Mg_{0.04}O$ nanoparticles obtained after Le-Bail refinement of X-ray diffraction pattern and compared with JCPDS card.

Sample name (Compared with JCPDS)	Cell Parameters				Crystallite size (nm)
	a=b	c	Volume	c/a	
JCPDS 089-1397 (P 63 m c)	3.253	5.213	47.77	1.6025	----------
$Zn_{0.95}Co_{0.05}O$	3.2467	5.2005	47.47	1.6018	14.45±1.53
$Zn_{0.91}Co_{0.05}Mg_{0.04}O$	3.2536	5.2102	47.76	1.6014	20.69±2.89
$Zn_{0.96}Mg_{0.04}O$	3.2485	5.2018	47.54	1.6013	18.68±3.04

$\alpha=\beta=90^o$, $\gamma=120^o$ and *a, b, and c are in* A^o

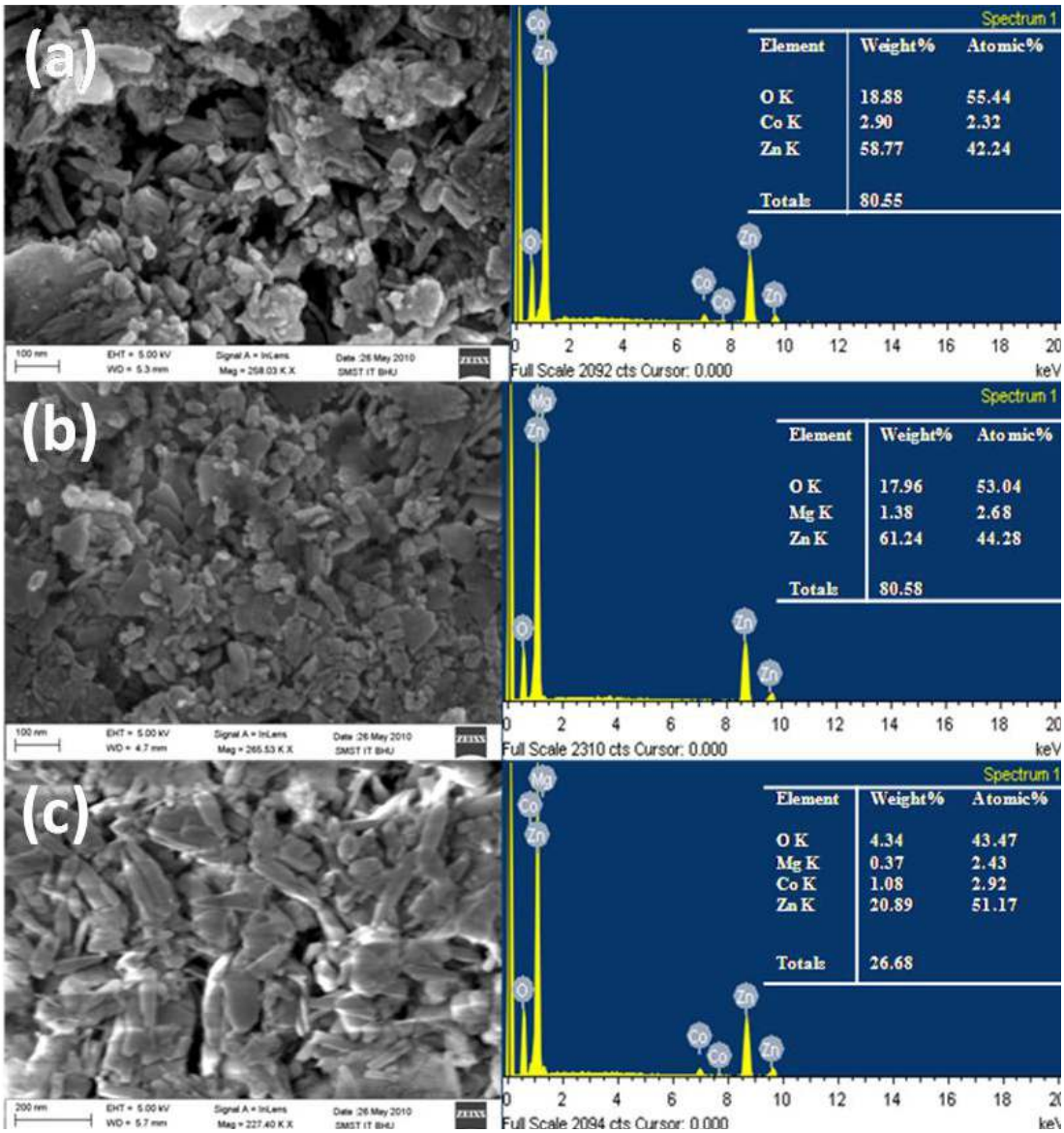

Figure 5.11: FE-SEM micrograph with corresponding EDX spectra of **(a)** $Zn_{0.95}Co_{0.05}O$ **(b)** $Zn_{0.96}Mg_{0.04}O$ and **(c)** $Zn_{0.91}Co_{0.05}Mg_{0.04}O$ nanoparticles.

5.2.2 Optical properties

The optical band gap energy (E_g) is determined from the absorption coefficient, α measured as a function of the incident photon energy E($h\nu$) using a UV-visible spectrophotometer. The linear portion of the curve is extrapolated and the band gap is calculated from $(\alpha h\nu)^2$ versus hν plot as shown in Fig. 5.12(a-d). The band gap of ZnO is found to be 3.28eV, which is increased to 3.35eV in case of Mg doped sample and further decreased to 3.17eV after doping with Co. As the band gap of MgO (~7.7eV) is higher than ZnO, it is

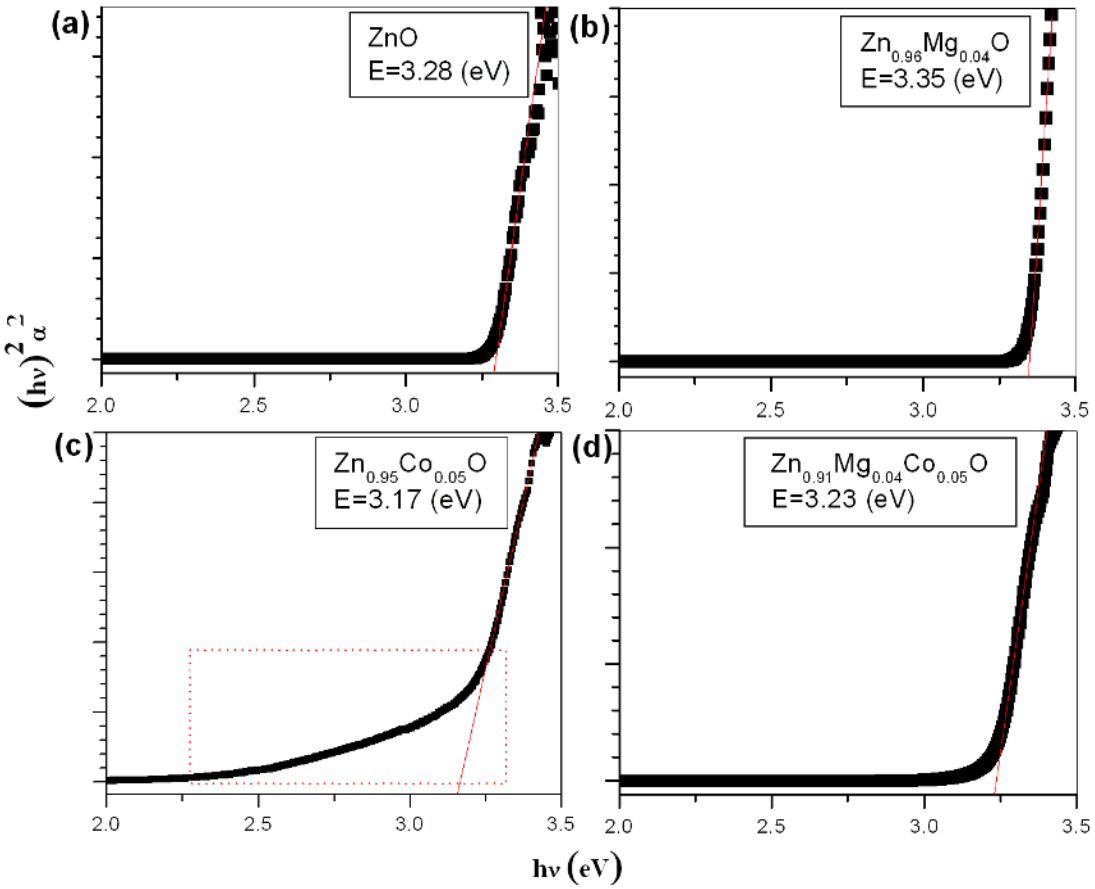

Figure 5.12: Plot of $\alpha^2(h\nu)^2$ vs. hv of $Zn_{1-x-y}Co_yMg_xO$ **(a)** x=0.0 and y=0.0 **(b)** x = 0.04 and y=0.0 **(c)** x=0.0 and y = 0.05 and **(d)** x = 0.04 and y =0.05.

expected higher band gap in Mg doped ZnO sample as we observed in the present case [Shan *et al*. (2004)]. Similarly, the band gap in Co doped ZnO sample is red shifted, analogous to the reported literatures [Xu *et al*. (2010)]. The red-shift in E_g is due to the sp-d exchange interactions between the band electrons and the localized d electrons of the Co^{2+} ions substituting Zn ions. The s-d and p-d exchange interactions lead to a negative and a positive correction to the conduction band and the valence band edges, resulting in a band gap narrowing. In Co and Mg codoped samples, the band gap energy (~3.23 eV) is intermediate between the band gap of Co and Mg doped samples, which is expected. Further, one may note that the UV-visible spectra of $Zn_{0.95}Co_{0.05}O$ clearly show a strong absorption in the sub-band-gap range (2.2–3.2 eV) related to the *d-d* crystal field splitting and the charge transfer

absorptions of Co [Samanta *et al*. (2006)], which we have marked as square in Fig. 5.12(c).

5.2.3 Detection of Vibrational Modes

Fig. 5.13 shows the Raman spectra of all four samples. Overlapping bands of the samples are deconvoluted into separate peaks by Lorenzian fitting without any background correction. A typical Lorenzian fitting for the Raman spectra of above samples are shown in Fig. 5.14(a-d). The assignments of Raman peaks of all samples are summarised in Table 5.3. The observed Raman modes in the samples are compared with the reported vibrational modes [Manjon *et al*. (2005); Decremps *et al*. (2002); Cusco *et al*. (2007); Pan *et al*. (2007)]. It is clearly seen that reported values of first order Raman modes such as A_1(TO), E_1(TO), E_2(high), A_1(LO), E_1(LO) and second order modes such as

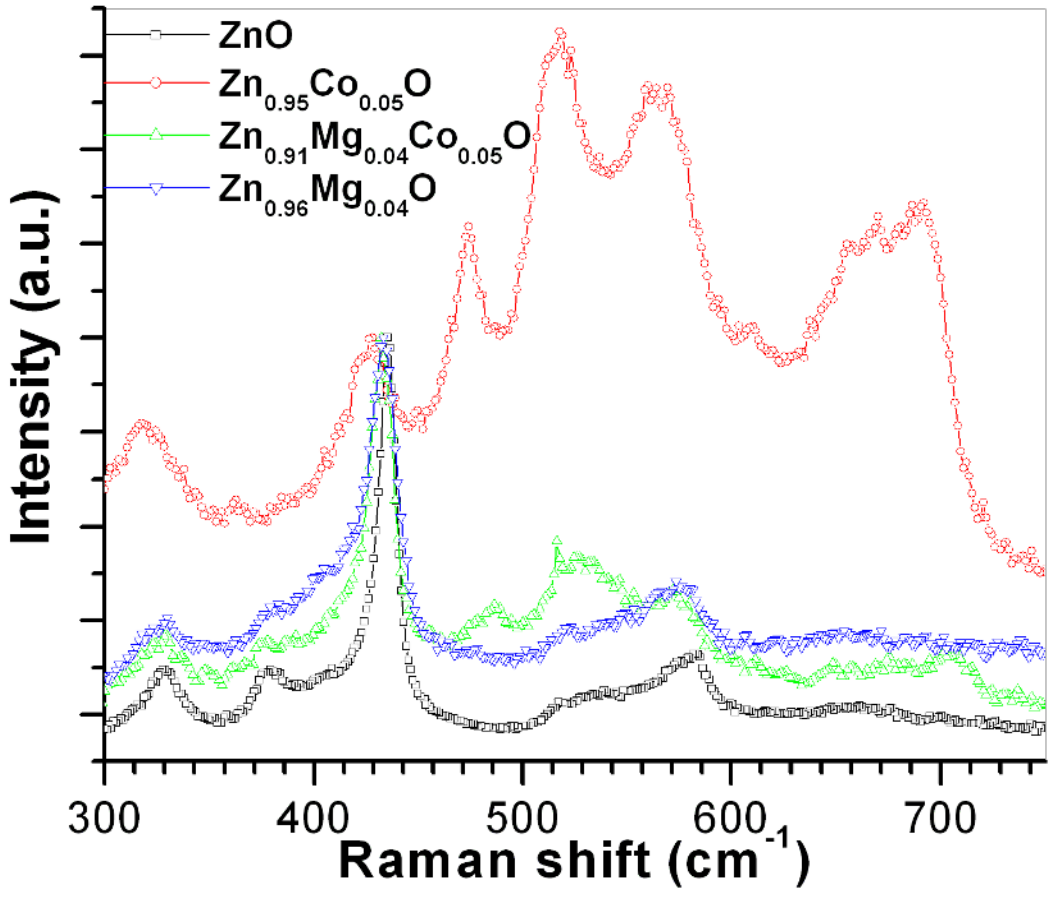

Figure 5.13: Normalised Raman spectra of $Zn_{0.95}Co_{0.05}O$, $Zn_{0.96}Mg_{0.04}O$ and $Zn_{0.91}$ $Co_{0.05}Mg_{0.04}O$ nanoparticles.

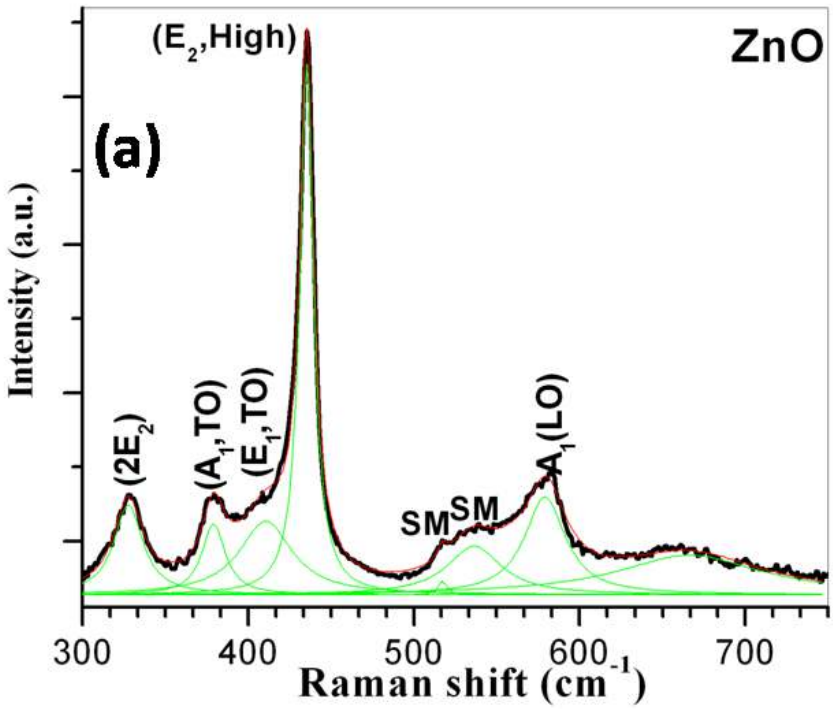
(a)
ZnO
(E2,High)
(2E2)
(A1,TO)
(E1,TO)
SM
SM
A1(LO)
Intensity (a.u.)
300
400
500
600
700
Raman shift (cm-1)

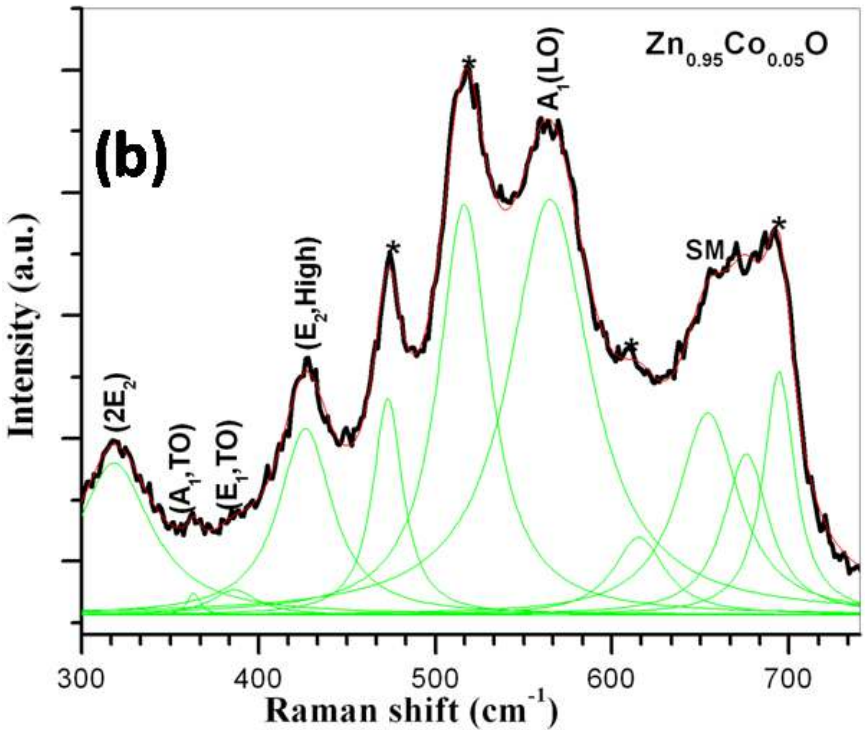
(b)
Zn0.95Co0.05O
A1(LO)
SM
(E2,High)
(2E2)
(A1,TO)
(E1,TO)
Intensity (a.u.)
300
400
500
600
700
Raman shift (cm-1)

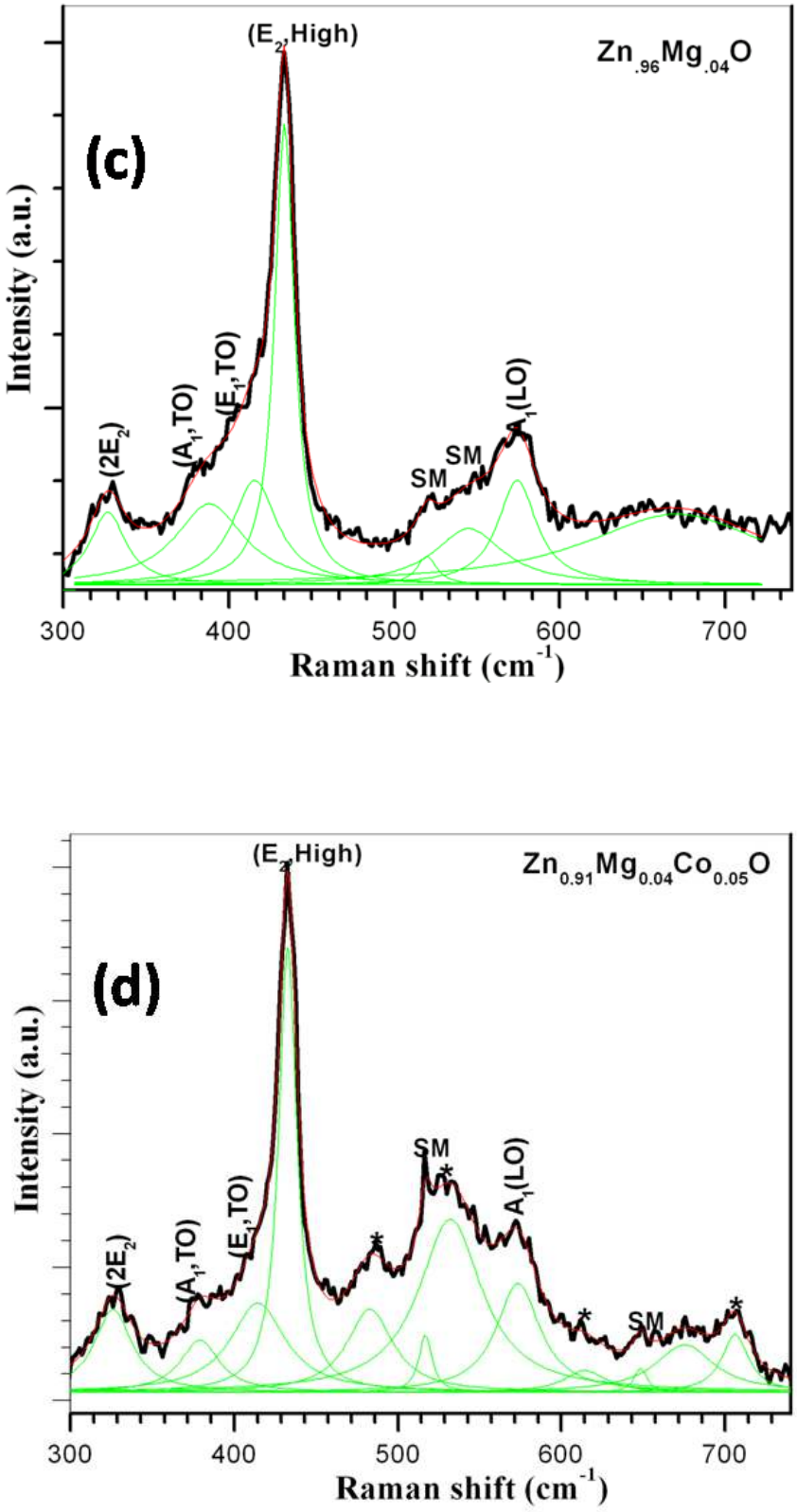

Figure 5.14: Lorentzian fitting for the Raman spectra of **(a)** ZnO, **(b)** $Zn_{0.95}Co_{0.05}O$, **(c)** $Zn_{0.96}Mg_{0.04}O$ and **(d)** $Zn_{0.91}$ $Co_{0.05}Mg_{0.04}O$ nanoparticles.

Table 5.3 Vibrational modes observed from Raman spectra of $Zn_{0.95}Co_{0.05}O$, $Zn_{0.96}Mg_{0.04}O$ and $Zn_{0.91}Co_{0.05}Mg_{0.04}O$ nanoparticles are compared with the reported vibrational modes of ZnO.

Raman Vibrational Modes of ZnO	Reported Raman Vibrational Modes of ZnO	Observed Raman Vibrational Modes of $Zn_{1-x-y}Mg_xCo_yO$			
		X=0.00 Y=0.00	X=0.04 Y=0.00	X=0.04 Y=0.05	X=0.00 Y=0.05
	1st order Raman Active Phonon Modes				
A_1(TO)	382‡,378†	379	380	378	363
E_1(TO)	414‡,410†	410	411	414	386
E_2^{high}	439‡,438†	434	433	432	426
A_1(LO)	574‡,574†	578	574	573	564
E_1(LO)	580‡,590†	-----	-----	-----	-----
	2nd order Raman Active Phonon Modes				
$2E_2$	333†	327	327	326	318
	Additional Modes				
$2B_2$(low)	520*	517	519	517	516
B_1(high)	552*	537	544	531	536
TA+B_1(high)	650*	-----	-----	649	654
Others	680§	670	673	674	676

[*Manjon *et al*. (2005); ‡Xu *et al*. (2006); †Samanta *et al*. (2006); §Duan *et al* (2010)] [*All Vibrational Modes are in* cm^{-1}]

$2E_2$ are matched well with the ZnO, Mg doped and Mg, Co codoped samples. However, Raman active phonon modes such as E_1 (LO) expected from the group theory are not seen in our measurement because of the backscattering geometry. In Co-doped ZnO sample all above Raman modes are shifted to lower wave number. The possible reasons for shifting of Raman peaks could be due to point defects, lattice strain and/or phonon confinement. Besides the first order and second order phonon modes of ZnO, a few more modes at 474, 516,

616, 654, 676 and ~694 cm^{-1} are observed in $Zn_{0.95}Co_{0.05}O$. It has been found that modes observed at 474, 516, 616 and 694 cm^{-1} are related with Co based complexes such as $Zn_yCo_{3-y}O_4$. These complexes can be similar to Co_3O_4 or $ZnCo_2O_4$ spinel structure [Sudakar *et al*. (2007)]. Samanta *et al*. (2007) have observed that in Co doped ZnO, Co ions are occupying Zn substitutional sites. The substitutions with more than 10% of Co exhibited additional Raman peaks in the spectra, suggesting the formation of the new phase, possibly $ZnCo_2O_4$ [Samanta *et al.* (2006)]. As per Hadjievl *et al*.'s (1988) report, Raman modes originating from Co_3O_4 phase are observed at 488, 522, 618 and 691 cm^{-1} which are same as observed in $Zn_{0.95}Co_{0.05}O$ and $Zn_{0.91}Mg_{0.04}Co_{0.05}O$ samples [Hadjiev *et al*. (1988)]. It is clear that the abrupt change of the Raman spectrum in $Zn_{0.95}Co_{0.05}O$ sample with respect to ZnO, is correlated with resonant process with the green excitation possibly of Co_3O_4 phase. This could be due to *d-d* transition of 'Co' in Co_3O_4 impurity phase, which further corroborates the absorption in sub-band region (Fig. 5.12(c)). Interestingly, the impurity phase is drastically reduced in $Zn_{0.91}Mg_{0.04}Co_{0.05}O$ as compared to $Zn_{0.95}Co_{0.05}O$. The Raman modes appeared in $Zn_{0.95}Co_{0.05}O$ and $Zn_{0.96}Mg_{0.04}O$ samples are also found in $Zn_{0.91}Mg_{0.04}Co_{0.05}O$ with different intensity. Here one may note here that besides the modes corresponding to Co_3O_4 phase, there are three additional modes observed at 519, 544 and 673 cm^{-1} in all samples with slight deviation. The peak at 516 cm^{-1} (assigned as additional mode) and 522 cm^{-1} ((F_{2g}) of Co_3O_4 phase) are merged into a single band in $Zn_{0.95}Co_{0.05}O$. Therefore, it is ambiguous to assign the whole band due to additional mode without extracting the individual peak. In order to confirm the presence of additional mode, we compare the intensity ratio of peak observed at 488cm^{-1} (E_g) and 522cm^{-1} (F_{2g}) of Co_3O_4 phase which is nearly 1:1 [Hadjiev *et al*. (1988)]. However, in $Zn_{0.95}Co_{0.05}O$ sample, the ratio of the above peaks is approximately 1:2. Hence, the increased intensity of 516/522 cm^{-1} in present case is due to the contribution of additional peak as well as Co_3O_4 phase. In our case however, the modes observed at 519, 544 and 673 cm^{-1} are mostly matched with the silent modes such as $2B_2$(low), B_1(high) and TA + B_1(high) respectively [Manjon *et al*.

(2005)]. These silent modes are independent of dopant type and concentration. The reason behind the observation of the silent modes is ascribed to the breakdown of the translational symmetry of the lattice caused by the host matrix defects rather than the impurities.

5.2.4 Magnetic Properties

Finally, magnetisation (*M*) as a function of temperature (*T*) at a fixed field of 1 Tesla was measured for $Zn_{0.91}Mg_{0.04}Co_{0.05}O$ sample and the results are shown in Fig. 5.15. The temperature dependent magnetisation shows identical behaviour under zero field cooling and field cooling, which eliminates the possibility of ferromagnetic behaviour within the measurement temperature range of 10-300 K. We measured the *M-H* curve with increasing and decreasing applied magnetic fields in the positive quadrant for the same sample at 10 K. The results are shown in Fig. 5.16(a-b). We do not see any hysteresis. The *M–H* curve obtained by increasing field is retraced while decreasing

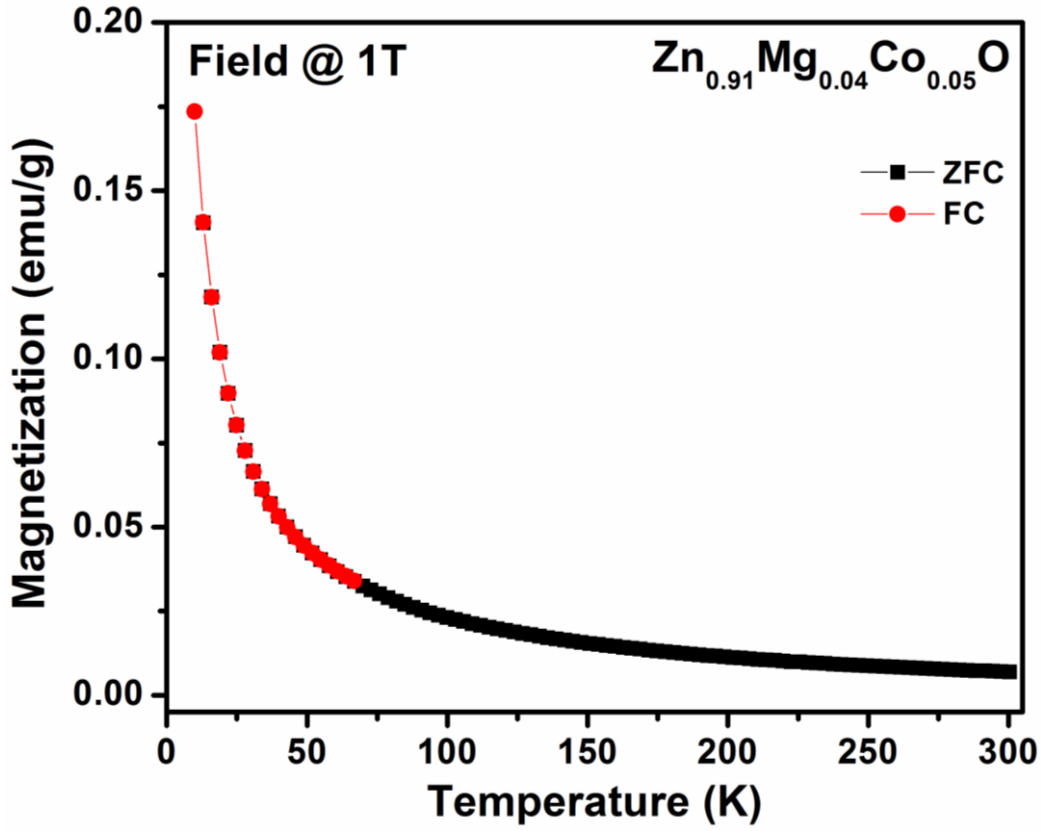

Figure 5.15: Temperature variation of magnetisation of the $Zn_{0.91}Co_{0.05}Mg_{0.04}O$ nanoparticles under field-cooling (FC) and zero-field-cooling (ZFC) conditions.

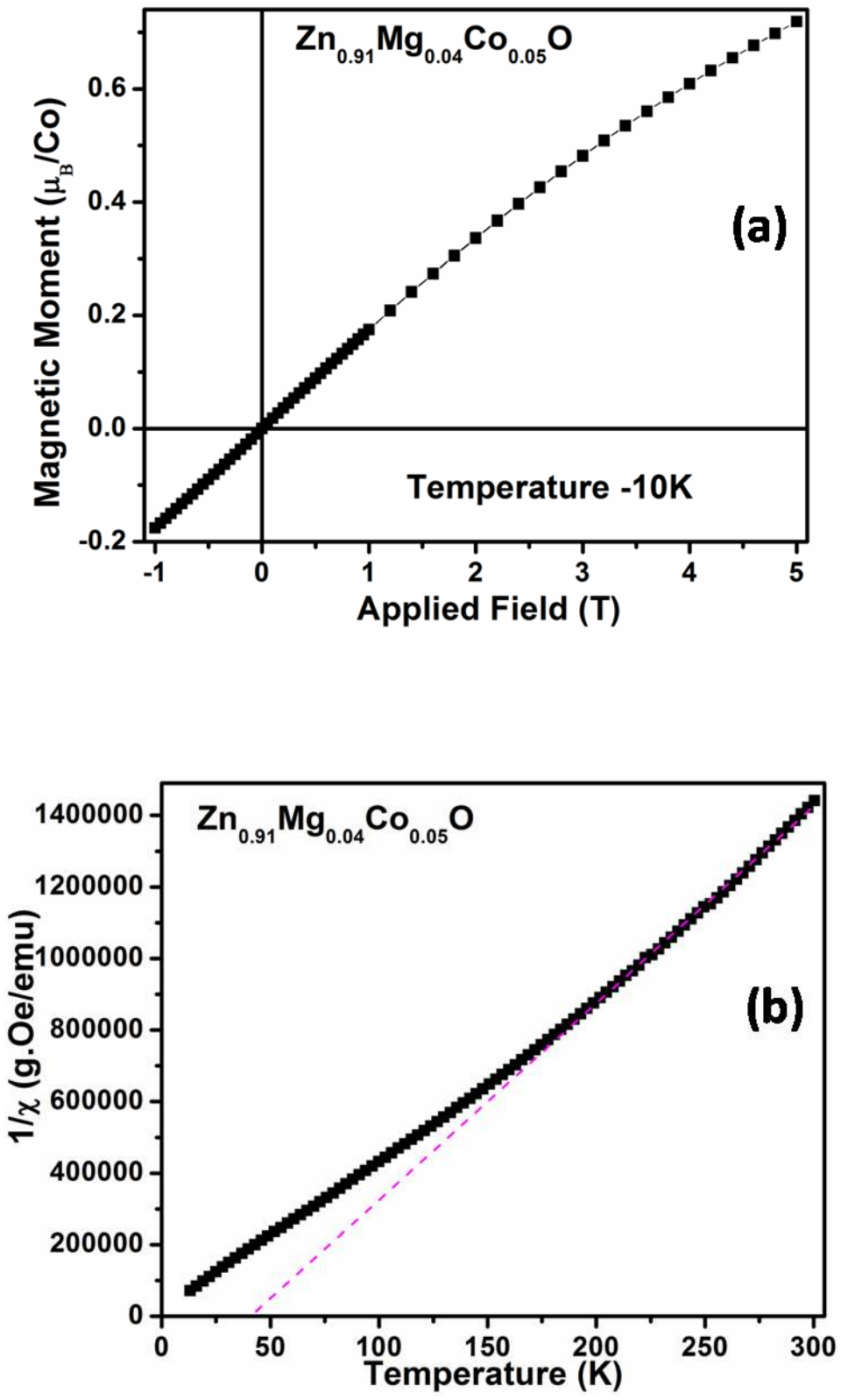

Figure 5.16: (a) Magnetisation versus external magnetic field of $Zn_{0.91}Mg_{0.04}Co_{0.05}O$. **(b)** Inverse of magnetic susceptibility as a function of temperature, which is extrapolated to zero in the temperature axis.

the field. This clearly indicates the absence of ferromagnetism. The magnetisation versus temperature plot (Fig. 5.15) seems to indicate characteristic paramagnetic behaviour, with a linear high temperature regime which is in agreement with our earlier report by Rath *et al*. (2009) for $Zn_{0.95}Co_{0.05}O$ sample. However, the extrapolation of the high temperature regime in the Curie-Weiss plot for $Zn_{0.91}Mg_{0.04}Co_{0.05}O$ sample, shown in Fig. 5.16(b), gives positive Curie-Weiss temperature, suggesting ferromagnetic correlations at low temperatures.

5.2.5 Detection of Cationic Defects

Further, we have carried out positron annihilation measurement to correlate the defects related additional Raman modes to the positron annihilation life times. It is well known that positrons preferentially populate (~and annihilate) in the regions where electron density, compared to the bulk of material, is lower (e.g. vacancy, vacancy clusters, and microvoids). The positron annihilation lifetime spectra (PAL) analysis of all three samples are best fitted with three lifetime components such as τ_1, τ_2, and τ_3 with relative intensities I_1, I_2, and I_3, respectively. Fig. 5.17 shows the recorded positron lifetime spectra and the fitted parameters are shown in Table 5.4. Positron life time component (τ_3) with intensity (~2%) yields a very long life time of the order of 3 ns which is due to the formation of orthopositronium formed in the intercrystalline regions characterised by a large free volume. The intermediate one, τ_2 and relative intensity I_2 is characteristic of positrons annihilation at the cluster of vacancy sites or larger defects or assigned to trapping of positrons in nanovoids at the intersection of three or more grain boundaries (e.g., triple junction) [Krause-Rehberg *et al*. (1999)]. The recent theoretical calculations and experimental works [Brauer *et al*. (2006); Dutta *et al*. (2005)] are used to scale the positron lifetime (τ_2) observed in present case. We found that these vacancy sites are made up of multiples of the Zn+O divacancies [Brauer *et al*. 2007]. Depending upon the size, vacancies could be a cluster of 2 to 6 di-vacancies (V_{Zn+O}) and the life time of positron annihilation also increases from

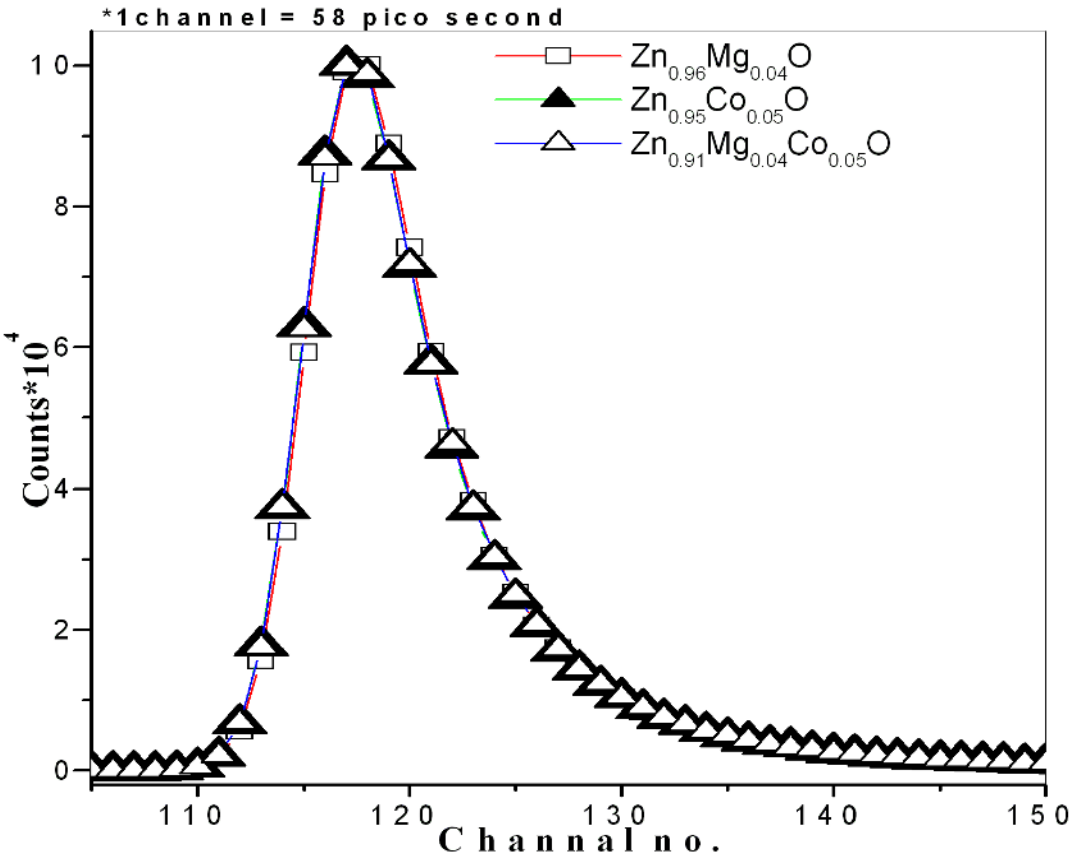

Figure 5.17: Positron lifetime spectra of $Zn_{0.95}Co_{0.05}O$, $Zn_{0.96}Mg_{0.04}O$ and $Zn_{0.91}$ $Co_{0.05}Mg_{0.04}O$ nanoparticles.

Table 5.4 Positron annihilation lifetimes of $Zn_{0.95}Co_{0.05}O$, $Zn_{0.96}Mg_{0.04}O$ and $Zn_{0.91}Co_{0.05}Mg_{0.04}O$ nanoparticles and corresponding intensities.

$Zn_{1-x-y}Mg_xCo_yO$ Powder sample	positron lifetime (ps)			Defect relative intensities		
	τ_1	τ_2	τ_3	I_1	I_2	I_3
X=0.00, Y=0.05	155.2±5.7	326.7±53	2939.6±119.4	40.5849±2.7	58.2611±2.7	1.154±.06
X=0.04, Y=0.05	158.3±5.7	329.9±5.2	3534.7±155.5	40.6119±2.7	58.5124±2.7	.8757±.05
X=0.04, Y=0.00	150.3±6.8	305.9±5.1	3088.5±121	36.2789±3.1	62.5861±3.1	1.135±.06

τ_1, τ_2, and τ_3 are positron life time with relative intensities I_1, I_2, and I_3

265 to 375 ps calculated theoretically by rigid lattice model [Chen *et al*. (2004)]. The 305-329 ps obtained for τ_2 in our case is well within the range of life time of positron annihilation corresponding to the cluster of (Zn+O) di-vacancies. The shortest lifetime, τ_1 with intensity I_1, corresponds to positron annihilation at structural defects in the grain boundaries. In bulk sample, τ_1 is ~158 ps and the lifetime in a Zn monovacancy is ~237ps [Tuomisto *et al*. (2003)]. One may note that τ_1 in our case is comparable to lifetime of positrons in defect free ZnO and less than life time of positron annihilation in Zn monovacancy. We conclude that in all three samples there is no evidence of Zn monovacancy rather cluster of (Zn+O) di-vacancies exist which could be responsible for the additional Raman modes observed in these samples.

5.3 Conclusions

$Zn_{1-x}Mg_xO$ (x = 0, 0.04, 0.08, 0.12, 0.10 and 0.15) and $Zn_{1-x-y}Mg_xCo_yO$ (x=0.04, y=0; x=0.04, y=0.05 and x=0, y=0.05) nanoparticles were synthesised by using conventional coprecipitation technique from equimolar solution of corresponding metal nitrates. No secondary phase was observed within the sensitivity of XRD. FTIR spectra demonstrated the presence of cationic vacancies in addition to unintentional hydrogen doping and their complexes in ZnO and Mg-H defect complex in $Zn_{1-x}Mg_xO$ ($0.04 \leq x \leq 0.20$). Positron life time measurement and photoluminescence studies confirmed that after Mg incorporation in ZnO lattice, the native defects were reduced or passivated by the hydrogen significantly in $Zn_{1-x}Mg_xO$ ($0.04 \leq x \leq 0.20$). XPS confirmed the excess hydrogen in Mg doped ZnO sample. Raman spectra of ZnO, $Zn_{0.96}Mg_{0.04}O$, $Zn_{0.95}Co_{0.05}O$ and $Zn_{0.91}Mg_{0.04}Co_{0.05}O$ revealed few additional modes corresponding to silent modes such as $2B_2$(low), B_1(high) and TA+B_1(high) of ZnO. From Positron annihilation life time measurement, the clusters of (Zn+O) di-vacancies were observed in ZnO, $Zn_{0.96}Mg_{0.04}O$, $Zn_{0.95}Co_{0.05}O$ and $Zn_{0.91}Mg_{0.04}Co_{0.05}O$ samples, which could be the origin of additional Raman modes. Raman study revealed the Co_3O_4 impurity in $Zn_{0.95}Co_{0.05}O$ and $Zn_{0.91}Mg_{0.04}Co_{0.05}O$ samples which is very difficult to detect with the help of XRD. Raman study revealed less Co_3O_4 impurity phase when Mg

is incorporated with Co in $Zn_{0.91}Mg_{0.04}Co_{0.05}O$ samples. In this study we observed ferromagnetic correlation at low temperature, although RT ferromagnetism was found to be absent. We conclude that while Mg incorporation in Zn site decreases the lattice defects and enhances the hydrogen storage capacity in $Zn_{1-x}Mg_xO$ ($0.04 \leq x \leq 0.20$). In $Zn_{0.91}Mg_{0.04}Co_{0.05}O$ the presence of Mg reduces the segregation of Co_3O_4 impurity phase.